

SAVERS: A Simulator of GNSS Reflections From Bare and Vegetated Soils

Nazzareno Pierdicca, *Senior Member, IEEE*, Leila Guerriero, *Member, IEEE*, Roberto Giusto, Marco Brogioni, *Member, IEEE*, and Alejandro Egido

Abstract—The mean power of the reflected Global Navigation Satellite System (GNSS) signals acquired by a GNSS-Reflectometry (GNSS-R) receiver can be modeled through the integral bistatic radar equation by weighting the contributions of all scatterers on the surface by the system impulse response. The geophysical properties of the scattering surface affect the magnitude of the reflected navigation signals through the bistatic scattering coefficient which, in case the observed surface is land, is a function of the soil dielectric properties, surface roughness, and vegetation cover. In this paper, the GNSS-R signal simulator developed in the framework of the Land MONitoring with Navigation signal (LEiMON) Project, supported by European Space Agency, is presented. The simulator is able to predict the power reflected by land, taking as input the system and observation parameters, as well as the land surface parameters. The latter are used to simulate both the coherent and the incoherent scattering, taking advantage of widely used theoretical models of bistatic scattering from bare soils and vegetated surfaces. First, the geometrical formulation is discussed, and then, the problem of polarization mismatch due to real antennas at circular polarization is faced following the polarization synthesis approach. Finally, a comparison with some experimental data collected during the LEiMON campaign is presented. The simulations display the same trend of the experimental data, thus showing that the simulator can be used as an efficient tool for the interpretation of GNSS-R measurements.

Index Terms—Bistatic scattering, electromagnetic models, Global Navigation Satellite System (GNSS)-Reflectometry (GNSS-R), soil moisture content, vegetation.

I. INTRODUCTION

IN THE last few years, the bistatic perspective opened up to microwave remote sensing of geophysical quantities. Bistatic radar systems can provide synergistic and complementary information with respect to conventional monostatic radar systems, potentially offering the optimal sensitivity to

biogeophysical parameters of the land surface [1], [2]. A passive radar is a valuable option, although there are constraints on the bistatic geometry related to resolution requirements [3], [4]. Among possible bistatic techniques, Global Navigation Satellite System (GNSS)-Reflectometry (GNSS-R) is particularly attractive since only receivers need to be deployed and a large number of transmitters are already in place as part of the GNSS network. This feature makes the technique intrinsically inexpensive and the instrumentation generally simpler and smaller with respect to active radar systems. The GNSS-R technique consists in detecting the signal of opportunity coming from one of the GNSS satellites and scattered off the Earth surface using an antenna looking down to the surface and possibly another one looking up to collect the incoming signal to use as reference. Exploiting the suitable modulation of the GNSS signal and a coherent detection, one can either measure the delay of the signal, to perform altimetry of the Earth surface, or its magnitude, to carry out scatterometric applications.

In the near future, the increasing number of GNSS satellite constellations will guarantee a wide coverage of the Earth surface, i.e., a large number of reflections that can be detected by a single GNSS-R receiver. Up to now, most of GNSS-R activities have been carried out over ocean, given the highly reflective characteristics of water. However, the low frequency band exploited by the navigation systems (i.e., typically L-band) would be suitable to land-oriented applications, such as soil moisture and vegetation biomass monitoring, due to the reduced atmospheric attenuation and especially the good penetration capability. Several experimental campaigns have recently demonstrated that the scatterometric observable is indeed sensitive to soil and vegetation physical parameters (see [5]–[10]); however, few theoretical studies have been dedicated to this application.

The first theoretical description of the Global Positioning System (GPS) reflected waveform measured by a receiver appeared in [11]. This model provides a fundamental theoretical framework for describing the data collected from a GNSS-R receiver, accounting for the structure of the GNSS signal and measurement geometry. However, it was conceived by the authors for the ocean, introducing the probability distribution function of sea slopes into the scattering coefficient that was modeled by means of the geometrical optics (GO) approximation. Subsequently, the same authors extended their work concerning GPS scatterometry over ocean to the case of a bare rough soil surface [12]. Due to its simple form, the GO has

Manuscript received February 1, 2013; revised August 12, 2013 and November 29, 2013; accepted December 13, 2013. Date of publication January 27, 2014; date of current version May 22, 2014. This work was supported by the European Space Agency under Contract AO/1-5830/08/NL/AF.

N. Pierdicca and R. Giusto are with the Department of Information Engineering, Electronics and Telecommunications, Sapienza University of Rome, 00184 Rome, Italy (e-mail: nazzareno.pierdicca@uniroma1.it; r.giusto@gmail.com).

L. Guerriero is with the Department of Civil and Information Engineering, University of Rome Tor Vergata, 00133 Rome, Italy (e-mail: guerriero@disp.uniroma2.it).

M. Brogioni is with the Istituto di Fisica Applicata/National Research Council (IFAC-CNR), 50019 Sesto Fiorentino, Italy (e-mail: m.brogioni@ifac.cnr.it).

A. Egido is with the Starlab, 08022 Barcelona, Spain (e-mail: alejandro.egido@starlab.es).

Color versions of one or more of the figures in this paper are available online at <http://ieeexplore.ieee.org>.

Digital Object Identifier 10.1109/TGRS.2013.2297572

been generally considered in the GNSS-R theoretical works developed up to now. This representation, excluding all Bragg effects, applies to rough surfaces with a large radius of curvature which can be locally approximated by tangent planes. It assumes that only incoherent scattering takes place from a set of specular points whose positions are determined by the occurrence of a specular reflection from the transmitter to the receiver. However, as described in the literature [13]–[15], the bistatic signal generally consists of both a coherent and an incoherent component. Indeed, according to recent studies [1], [16], the coherent scattering from a rough surface, concentrated around the specular direction, can be comparable or can even overpass incoherent scattering when the observed surface is characterized by small scale roughness with respect to wavelength.

Theoretical tools capable of reproducing both the coherent and the incoherent power measured over land surfaces by a GNSS-R receiver have not yet been developed and validated. In this paper, the simulator developed in the framework of the Land MONitoring with Navigation signal (LEiMON) project [10], supported by ESA, is presented. The experimental activity carried out during LEiMON provided a good data set to test the simulator. It exploited a receiver, developed by Starlab, acquiring GPS Coarse/Acquisition (C/A) coded signal. As a whole, the implemented software is capable of simulating the output of the GNSS-R cross-correlation process of the reflected and direct signals taking into account the system parameters, the observation parameters, and the surface parameters. Two main modules can be distinguished in the simulator architecture: the electromagnetic module and the signal simulator. The rationale of this distinction stems from the fact that the electromagnetic model predicts the bistatic scattering coefficient of the surface target, which describes the fundamental electromagnetic interaction phenomena, whereas the signal simulator is capable of reconstructing the real measurements of the instrument resulting from the tracking and detection processing steps, which are functions of time and Doppler frequency. The simulator output can be represented in the form of a waveform or a delay–Doppler map (DDM) retrieved by a nadir-looking GPS receiver on board a platform at a given height, steady or flying at a given speed. As a preliminary validation of the developed software, a subset of the LEiMON campaign data set was used to display the effects of observation angle, soil moisture, roughness, and vegetation, as shown by the experiment and predicted by the simulator. As it will be better explained later on, in the LEiMON ground-based case, only one point of the DDM is relevant, but the full capability of the simulator is described in this paper.

Section II describes the structure and the main features of the signal simulator. The electromagnetic modules, which are called by the simulator and are based on consolidated formulations, are summarized in Section III. Because of the circular polarization of the GNSS signal, a particular attention is devoted to the problems of polarization mismatch and crosstalk isolation in the prediction of the actual measurements. Finally, the LEiMON experimental data are exploited in Section IV, as a reference to compare with the outputs of the simulator in the specific conditions of the experiment.

II. SIMULATOR DESCRIPTION

The Soil And VEgetation Reflection Simulator (SAVERS), which has been developed during the LEiMON project [17], is based on the theory described in a fundamental work in [11]. Here, the expression given in [18] is reported since it makes apparent the relationship with the bistatic radar equation. The power output of the signal correlator as a function of the time delay τ and of the Doppler shift f , i.e., the so-called DDM, is

$$|Y_{rt}(\tau, f)|^2 = \frac{\lambda^2}{(4\pi)^3} P_T T_i^2 \int \int_A \frac{G_T(\theta_i, \phi_i) G_R(\theta_s, \phi_s)}{R_R^2 R_T^2} \times \sigma_{rt}^0(\theta_i, \phi_i; \theta_s, \phi_s; \Theta) \Lambda^2(\delta\tau) S^2(\delta f) dA \quad (1)$$

with P_T being the transmitted power of the GNSS satellite, λ being its wavelength, and G_R and G_T being the receiving and transmitting antenna gains, respectively. The integration area A is chosen much larger than the receiver antenna footprint but can practically coincide with the glistening area or be limited by either the antenna beamwidth or the signal coding, as in the case of a beam-limited or a pulse-limited system, respectively. R_T and R_R are the distances of the differential area dA from the transmitter and receiver.

Equation (1) originates from cross-correlating the received signal with a replica of the transmitted pseudorandom noise (PRN) codes along the coherent integration time T_i and absolute squaring the cross-correlation output. It shows that the measurements depend on instrument characteristics, such as receiver antenna pattern and impulse response functions in time and frequency domains (Λ^2 is the *triangle* function for the GPS C/A code, and S is the *sinc* function), and on the target bistatic scattering coefficient σ_{rt}^0 (subscript r and t indicate the polarizations of the received and transmitted signals). The latter is a function of the incidence (θ_i, ϕ_i) and scattering (θ_s, ϕ_s) angles and target geometric and dielectric properties included in the vector parameter Θ . In (1), we formally combine the coherent component together with the incoherent one so that, as for the coherent component, vector Θ includes further parameters, such as antenna distances and beamwidth, as it will be explained later on. Moreover, measurements depend on receiver, transmitter, and target relative positions and velocities, which affect signal delay and Doppler shift. Specifically, $\delta\tau$ and δf are the differences between the sampled time delay τ , or sampled frequency f , and a reference delay and Doppler frequency.

SAVERS was developed in Matlab and Fortran; the main modules and data flow are depicted in Fig. 1. We distinguish a geometric module, a DDM module, i.e., the core of the system implementing (1), and two modules computing the bistatic scattering coefficient for bare soil and vegetated soil. The last two modules are developed in Fortran and integrated into the Matlab main program as Matlab EXecutable functions. At the time of writing, the model for sunflower was implemented, in order to reproduce the data collected during LEiMON.

The identification of the point of specular reflection of the GNSS signal on the Earth surface is the first step of the processing chain. The satellite position at the time of the measurements is computed by propagating satellite ephemerides from the GPS

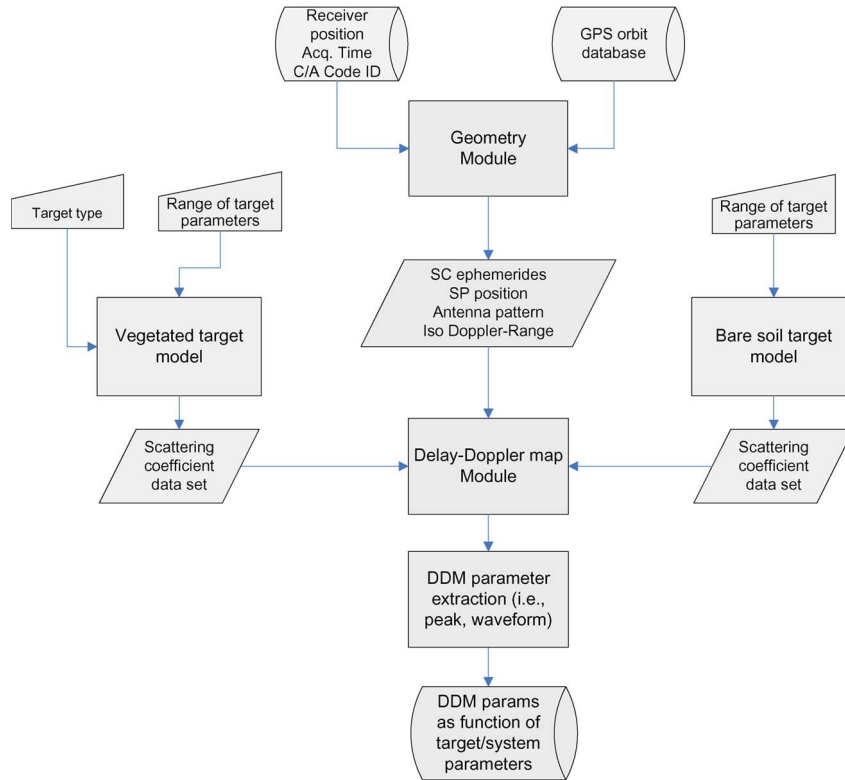


Fig. 1. Simulator main functions and data flow.

Yuma Almanach. Provided the receiver position, the specular point position is computed according to standard procedures.

In SAVERS, the surface over which the integral is performed is assumed to be locally flat. The local reference system xyz (local frame) is centered in the specular point, with z -axes along the geodetic vertical and the xz plane coincident with the specular reflection plane. The local frame defined here is similar to the standard local East, North, Up system. The z -axis of our local frame coincides with the Up axes, whereas the x -direction is rotated with respect to the local East direction to incorporate both the transmitter and receiver, thus making the xz plane correspondent to the incidence plane and $\phi_i = 0$. As the receiver movement is supposed to be given as a heading (with respect to North) and an inertial velocity, the Earth rotation is accounted for to refer the receiver velocity to the local frame.

For each point xy of a regular grid over the surface, the software computes the scattering direction (zenith θ_s and azimuth ϕ_s angles) toward the receiving antenna, the ranges from the receiver to the point, and the Doppler shift (based on transmitter and receiver speed). The latter is referred to the Doppler of the direct signal collected by the up-looking antenna, as generally done in the processing of GNSS-R raw data. The range from the transmitter to surface targets and the incidence direction are assumed equal for all the surface grid points given the large distance of the GPS satellites from the surface. The aforementioned angular quantities, $\theta_i, \theta_s, \phi_s$, allow the electromagnetic module to compute the bistatic scattering coefficients in each point of the surface. The receiver antenna gain is inserted into the radar equation as a function of the point looking angle assuming a cosinusoidal pattern (the antenna beamwidth being provided by the user). The gain of

the transmitter antenna is not considered since the incident power flux density is assumed constant within the integration area, and it cancels out when the signal from the down-looking antenna is normalized to that of the up-looking antenna, as discussed later on (see Section III-B). All quantities are then combined by the bistatic radar equation within regular intervals of time delay and Doppler shift, in order to build the DDM.

SAVERS performs several runs for different positions of the GPS transmitter along its orbit, spanning a time interval selected by the user, thus producing results for different incidence angles. The user provides the PRN number of the satellite whose reflection is to be simulated and also the description of the soil surface and, in case, of the vegetation to be used in the electromagnetic module. For each run, SAVERS produces a number of plots with either intermediate quantities (see Figs. 2–4), the final DDM (one example is displayed in Fig. 5), and the waveform, plus an output file containing the DDM and the waveform values for all the transmitter positions. Also, the possibility to produce in output the magnitude of the waveform peak as a function of the incidence angle has been foreseen, in order to simulate the LEiMON experimental data [10], as it will be shown in the following sections. Indeed, the waveform acquired by a ground-based receiver spans only one chip so that looking at its peak is sufficient for the purpose of comparison with LEiMON data.

The simulation which produced Fig. 2 refers to a receiver at a height of 10 km, flying at a speed of 180 m/s, heading North, and with an antenna 3-dB beamwidth of 60° . The specular point position is in the origin of the coordinates, and the incidence angle is $\theta_i = 31.4^\circ$. It is worth to comment this intermediate graphical output to clarify how SAVERS works and to check the

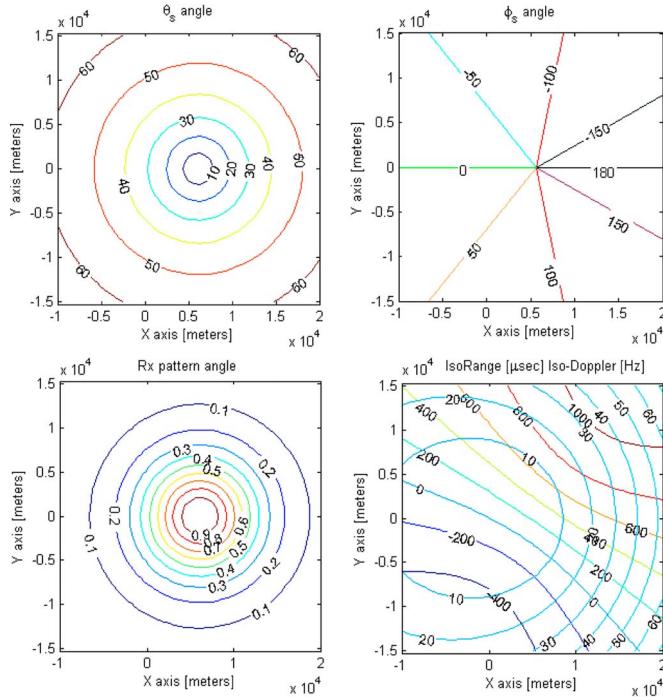


Fig. 2. Simulator geometrical output plots in the surface local coordinates xy . Receiver height = 10 km, receiver velocity = 180 m/s, heading = 0° , antenna beamwidth = 60° , and incidence angle = 31.4° . Top left: Zenith scattering angle θ_s . Top right: Azimuth scattering angle ϕ_s . Bottom right: Isodelay (in μ s) and iso-Doppler (in Hz) lines. Bottom left: Antenna gain pattern.

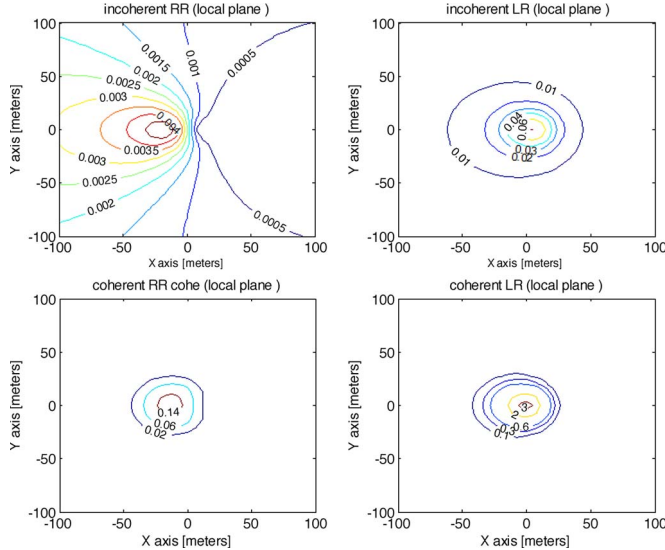


Fig. 3. Bistatic scattering coefficient σ^0 , in the surface local coordinates xy , of a bare soil with moisture content SMC = 20%, roughness standard deviation $\sigma_z = 0.5$ cm, and correlation length $\ell = 5$ cm. Antenna beamwidth = 50° . Other input parameters as in Fig. 7. Top left: Incoherent RR polarization. Top right: Incoherent LR polarization. Bottom right: Coherent RR polarization. Bottom left: Coherent LR polarization.

correctness of the results. The upper left plot shows the scattering zenith angle in the local reference frame. At coordinate (0, 0), the scattering angle is around 30° – 35° , as expected, since, at the specular point, the incidence and zenith scattering angles must be the same. The upper right plot shows the azimuth scattering angle. For a very distant transmitter illuminating all the surface points from the same direction (as assumed by

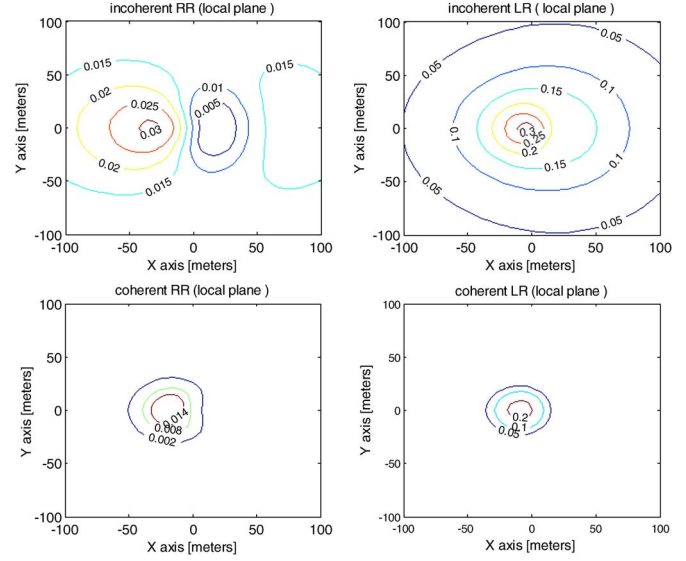


Fig. 4. Bistatic scattering coefficient σ^0 , in the surface local coordinates xy , of a bare soil with moisture content SMC = 20%, roughness standard deviation $\sigma_z = 3$ cm, and correlation length $\ell = 5$ cm. Antenna beamwidth = 50° . Other input parameters as in Fig. 7. Top left: Incoherent RR polarization. Top right: Incoherent LR polarization. Bottom right: Coherent RR polarization. Bottom left: Coherent LR polarization.

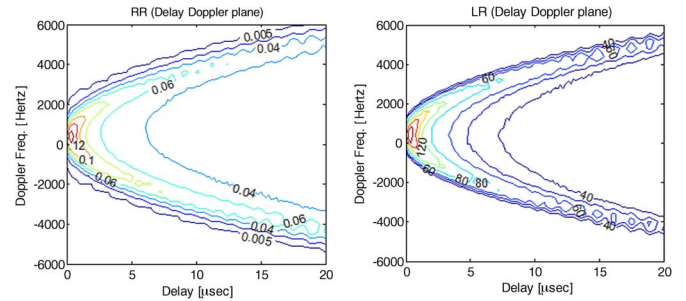


Fig. 5. DDM of incoherent power at (left) RR and (right) LR polarizations scattered by a bare soil with moisture content SMC = 20%, roughness standard deviation $\sigma_z = 1.5$ cm, and correlation length $\ell = 5$ cm. Receiver height = 700 km, receiver velocity = 7500 m/s, heading = 0° , antenna beamwidth = 60° , incidence angle = 13° , and $P_T G_T = 10^{25}$ W.

SAVERS) and with the x -axes aligned toward the receiver on the specular reflection plane (again a simulator condition), the scattering azimuth of the specular point is 0° . This is true also for all the points lying between the transmitter and the receiver along the x -axes. The points aligned along the x -axes, but far from both the transmitter and the receiver, have an azimuth of 180° . Finally, an azimuth scattering angle of $\pm 90^\circ$ should be associated to all points aligned along a straight line parallel to the y -axes and passing through the receiver location. All these conditions are correctly reproduced in the plot. The bottom left plot of Fig. 2 represents the antenna gain pattern. The maximum of the antenna pattern coincides with the receiver position in the xy local frame since the simulator assumes a nadir-pointing antenna, as in the LEiMON experiment. The specular point should be at about $h \cdot \tan \theta_i \sim 6$ km from the receiver; in fact, the center of the antenna pattern is at $y = 0$, and at coordinate x slightly greater than 5 km. Note that the isoline labeled 0.5 delimits the 3-dB antenna footprint. The bottom right plot of Fig. 2 shows the isorange and iso-Doppler lines

above the Earth surface. The isorange lines are ellipses around the specular point, with the latter located at coordinate (0, 0) and corresponding to the point of minimum delay. The correctness of the geometry can be verified against simplified formulas, such as those in [19]. From the aforementioned figure, the semiaxes of the isoline at a delay of 10 μ s are a bit less of 10 and 9 km, as compared to 9.7 and 8.3 km, respectively, as derived from [19]. The iso-Doppler lines are hyperbolas whose axis is expected to be approximately parallel to the receiver velocity in an Earth-fixed reference frame since such velocity is much larger than the GPS transmitter velocity [20].

Figs. 3 and 4 report the bistatic scattering coefficient σ^0 for each cell on the surface, which has been assumed as a bare soil in these plots, for RR (left column) and LR polarizations (right column). The input observation and system parameters are those of the LEiMON experiment. The soil is characterized by soil moisture content SMC = 20%, and the roughness standard deviation is $\sigma_z = 0.5$ cm in Fig. 3 and $\sigma_z = 3$ cm in Fig. 4. These plots will be recalled in Section IV to interpret the LEiMON data with the aid of SAVERS; then, here, we draw some general remarks.

The peak of sigma nought values is observed around $x = 0$ and $y = 0$, which are the coordinates of the specular point on the local plane, meaning that the maximum power is directed along the specular direction, particularly for the coherent component (bottom row), as expected. Comparing the two figures, it is possible to observe that the incoherent σ^0 values are larger for the rough surface, while the coherent component has larger values when the soil is smooth. Furthermore, the incoherent scattering of a rough surface extends over a wider area.

Fig. 5 reports the DDMs, i.e., the output of the signal correlator $|Y_{rt}(\tau, f)|^2$ for the RR- and the LR-polarized incoherent scattering, produced by the simulator in correspondence to a soil surface observed by a spaceborne receiver at an incidence angle $\theta_i = 13^\circ$. Although the ground-based configuration of the LEiMON experiment yields DDMs spanning a single delay and Doppler sample, we present this result to show all SAVERS capabilities. In particular, the spaceborne case has been considered here in order to reproduce the typical horseshoe pattern of DDMs collected over the sea surface. Note that this pattern is produced when collecting incoherent scattering from a large glistening zone so that, in case of land scattering, when the coherent component can be important, as well as with low altitude receivers, this distinctive shape cannot be observed.

III. ELECTROMAGNETIC MODELS

The theoretical expression in (1) shows that the scattered GNSS-R signal contains the Earth surface signature through the bistatic scattering coefficient $\sigma_{rt}^0(\theta_i, \phi_i; \theta_s, \phi_s; \Theta)$. Since the adopted scattering models are extensively described in the literature and were already implemented (see [1], [2], [21], and [22]), here, we only summarize them. Conversely, we will provide more details on the treatment of the circular polarization issue, specific for the GNSS-R, in the next section and in the Appendix. In order to completely characterize the properties of the scattered wave, we will take into account both coherent and incoherent scattering processes.

The simulation of the soil incoherent contribution requires an analytical model of bistatic scattering which can be selected among the available approximations on the basis of the ratio of the soil roughness parameters against the operational wavelength. In this paper, the integral equation model, in its advanced (AIEM) formulation [23], was adopted for the soil surface. More details on the implementation of AIEM included in SAVERS are provided in [21], together with some validation results that support the choice of this analytical model. We just mention here that the IEM iterates into the surface field integral equation the Kirchhoff approximated solution up to the second order. This leads to a scattering coefficient of the incoherent component that includes two additional terms, the complementary and the cross terms, which add to the traditional Kirchhoff term. In this way, the range of validity of the solution in terms of roughness standard deviation and correlation length extends beyond that of the GO and Physical Optics solutions and comprises that of the Small Perturbation Method approximated solution [21].

The coherent component produced by scattering from a rough surface is described in the literature following two different approaches. The first one [14] considers the incident wave as a plane wave which is bounded to account for the limited antenna beamwidth, while the other [24] considers the sphericity of the incident wavefront. Here, the formulation of the coherent scattering coefficient proposed by Fung and Eom [24] has been selected since it correctly takes into consideration the spherical shape of the wavefront which is produced in the far-field zone by a real antenna with a fairly wide main lobe. The assumption of an incident plane wave can be valid for computing the incoherent component since the incident wave can be considered a plane one within a random surface correlation length, but this is not true for the coherent component which is associated to an extended mean plane surface. On the other hand, the assumption of a spherical wave, impinging on a surface in the far field of the antenna, is justified in most cases. For instance, in the LEiMON experiment, the far zone condition applies for distances larger than about 1.3 m, which is much smaller than the surface target distance. The Eom and Fung formulation formally introduces for the coherent component an “equivalent” scattering coefficient which, as opposed to the one defined for a random surface, is a function of the antenna beamwidths and distances, which, in (1), are comprised in the parameter vector Θ . The equivalence of this approach with the image theory is demonstrated in [24, Eq. (8)], to which the reader is referred for details.

Land surfaces are often covered by vegetation which interacts with the L-band electromagnetic wave of the impinging GNSS signal. It is therefore necessary to take into account vegetation dielectric and morphological properties in order to model the attenuation and scattering of the land cover. In this paper, the Tor Vergata model has been included in the GNSS-R signal simulator [2], [22]. It is a discrete microwave scattering model which uses the radiative transfer theory to characterize interactions between incoming electromagnetic waves and vegetation cover. The agricultural canopy has been schematized as a three-layer medium: the top layer containing leaves and twigs, the middle layer containing the vertical stems, and the bottom

layer representing the underlying rough soil. The generalized Rayleigh–Gans approximation [25] has been applied to model the bistatic scattering cross section and the extinction cross section of leaves and twigs, which are represented by randomly oriented dielectric thin disks and needles. The infinite cylinder approximation [26] has been applied to model the electromagnetic parameters of stems, which are represented by vertical cylinders.

The scattering and transmission properties of the canopy are integrated over the vegetation layer by applying the matrix doubling technique [25], thus including multiple scattering between the vegetation layer and the soil. The realistic distribution of dimensions and orientations is chosen depending on the stage of vegetation development. Like other physical models, the Tor Vergata model requires many inputs concerning soil parameters and scatterer dimension, geometry, orientation, and moisture content. However, in order to reduce the number of input parameters, the model includes a vegetation growth algorithm, i.e., empirical relationships between the various model input parameters and the plant height of some specific agricultural species, which were developed taking advantage of the experience gained in past ground campaigns [22] and of the *in situ* measurements carried out during LEiMON. This allows to constrain the simulations, reproducing the actual phenological condition of the considered vegetated target in various growing stages.

The scattering of microwaves by surfaces and by lossy objects depends, among others, on the dielectric constant of the media themselves. In this paper, a semiempirical model, presented in [27], which is based on a dielectric mixing approach and validated by an extensive set of experimental data, is used for soil. As far as the dielectric constant of vegetation is concerned, the semiempirical model proposed in [28] has been implemented. The latter is physically based in that it includes significant parameters, such as plant gravimetric moisture, free-water fraction, bound-water fraction, and free-water ionic conductivity. The values of these parameters were simply derived by fitting experimental data.

The dielectric constants, roughness parameters, and vegetation statistical parameters are assumed horizontally homogeneous within the resolution cell of the instrument, the latter being determined by the signal chip footprint or the receiver antenna footprint, respectively for a pulse-limited or a beam-limited system, as well as Doppler limited (particularly for long coherent integration time). This is accounted for by the SAVERS software through the consideration of the antenna footprint and both time and frequency domain impulse responses.

As previously mentioned, the scattering models were already described in the literature, whereas the treatment of the polarization issue within SAVERS is something new in the frame of GNSS-R signal simulation, and it is worth to be detailed. In order to account for the actual polarization of both transmitting and receiving antennas, which, in the case of GPS signals, are nominally circular, the polarization synthesis approach has been followed [29]. It allows the calculation of the power received at any combination of receiving and transmitting antenna polarizations, given the full Muller matrix provided by

the scattering models summarized before, which were therefore implemented in their fully polarimetric configuration.

A. Polarization Mismatch and Receiver Crosstalk Effects

It is well known that, when dealing with real antennas and/or dual-polarized reception systems, polarization mismatch and/or crosstalk between antenna channels can affect the measurements. Those effects are seldom included in the interpretation of GNSS-R signals, and for off-the-shelf devices, as in instruments used in the LEiMON experiment, their characterization is not as accurate as one may expect. In the following, we propose a method which is based on the polarization synthesis and aims at an evaluation of these effects, at least for a simplified receiver antenna model. This consideration may also apply to the transmitting antenna, but we disregard this possibility for the moment.

Introducing the correct polarization state of the antenna, the “*real*” scattering coefficients $\sigma_{RR}^{0'}$ and $\sigma_{LR}^{0'}$ of the observed surface measured by a “*nominal*” right circular R or left circular L antenna can be computed. Some background is reported in the Appendix, to which we refer for the meaning of the symbols introduced hereinafter. Considering the real receiving antennas made of a pair of electrical dipoles (with polarization unit vectors of (13) in the Appendix), after the application of polarization synthesis of (8) in the *backscattering alignment* (BSA) convention, we obtain the following:

$$\begin{aligned}\sigma_{LR}^{0'} &= \frac{2\pi}{A(1 + \cos^2 \theta_s)} \\ &\quad \times \left\langle |S_{vv} \cos \theta_s + S_{hh} - \iota(S_{vh} \cos \theta_s - S_{hv})|^2 \right\rangle \\ &= \frac{2\pi}{A(1 + \cos^2 \theta_s)} \\ &\quad \times \left\langle |S_{LR}(\cos \theta_s + 1) + S_{RR}(\cos \theta_s - 1)|^2 \right\rangle \\ \sigma_{RR}^{0'} &= \frac{2\pi}{A(1 + \cos^2 \theta_s)} \\ &\quad \times \left\langle |S_{vv} \cos \theta_s - S_{hh} - \iota(S_{vh} \cos \theta_s + S_{hv})|^2 \right\rangle \\ &= \frac{2\pi}{A(1 + \cos^2 \theta_s)} \\ &\quad \times \left\langle |S_{LR}(\cos \theta_s - 1) + S_{RR}(\cos \theta_s + 1)|^2 \right\rangle \quad (2)\end{aligned}$$

where we have used (9) and an ideal right-polarized wave has been assumed for the transmitted signal impinging upon the surface. The equations above can be computed using the elements of the Muller matrix of (10) provided by the electromagnetic models. Equation (2), expressed in terms of S_{LR} and S_{RR} , shows that the scattering coefficient measured by a real antenna combines contributions coming from LR and RR nominal scattering terms.

An additional error can be due to a nonideal cross-polarization isolation of the receiving channels which makes a fraction α of the signal go into the wrong polarization channel. By developing the polarization synthesis expressed as in (16), still considering a real receiving antenna made of a pair of

electric dipoles as in (13), we again obtain the “real” scattering coefficients as functions of the terms $\langle S_{pq} S_{mn}^* \rangle$ of the Muller matrix

$$\begin{aligned}\sigma_{LR}^{0'} &= \frac{2\pi}{A(1+\cos^2 \theta_s)} \left\langle |S_{vv} \cos \theta_s + (1-2\alpha)S_{hh} \right. \\ &\quad \left. - \iota [S_{vh} \cos \theta_s - (1-2\alpha)S_{hv}]|^2 \right\rangle \\ &= \frac{2\pi}{A(1+\cos^2 \theta_s)} \left\langle |S_{LR} [\cos \theta_s + (1-2\alpha)] \right. \\ &\quad \left. + S_{RR} [\cos \theta_s - (1-2\alpha)]|^2 \right\rangle \\ \sigma_{RR}^{0'} &= \frac{2\pi}{A(1+\cos^2 \theta_s)} \left\langle |S_{vv} \cos \theta_s - (1-2\alpha)S_{hh} \right. \\ &\quad \left. - \iota [S_{vh} \cos \theta_s + (1-2\alpha)S_{hv}]|^2 \right\rangle \\ &= \frac{2\pi}{A(1+\cos^2 \theta_s)} \left\langle |S_{LR} [\cos \theta_s - (1-2\alpha)] \right. \\ &\quad \left. + S_{RR} [\cos \theta_s + (1-2\alpha)]|^2 \right\rangle. \quad (3)\end{aligned}$$

B. Effect of Polarization Mismatch and Crosstalk: An Example

The effects of receiver polarization mismatch and crosstalk are here evaluated taking as reference the measurements of the GPS signal acquired at different incidence angles in a single day of the LEiMON campaign. During this experiment, the GNSS-R receiver was placed on a ground-based platform at a height of 25 m above the ground, equipped with antennas of 100° beamwidth. The measurements collected during this experiment were normalized to the signal received by the up-looking antenna [10]. Therefore, in order to make the comparison, in SAVERS, the GNSS-R signal computed by (1) has been normalized to the following correlator output:

$$|Y_{RR}^{UP}|^2 = PLF^{UP} \frac{\lambda^2}{(4\pi)^2} T_i^2 P_T \frac{G_T(\theta_i) G_R(\theta_i)}{R_{TR}^2}. \quad (4)$$

PLF^{UP} is the polarization loss factor of the up-looking antenna, which accounts for its polarization loss (see the Appendix). The direction of the impinging radiation from the very far GPS transmitter has been assumed equal to θ_i , and the gain of the up-looking antenna has been considered symmetric in azimuth and equal to the down-looking one since, in LEiMON, the two devices are identical. R_{TR} is the distance between the transmitter and the receiver. Similarly to the procedure described in the Appendix and in the previous section, PLF^{UP} results to be

$$PLF^{UP} = \left| \left((1-\alpha)\mathbf{p}_R' + \alpha\mathbf{p}_L' \right) \cdot \mathbf{p}^w \right|^2 = \frac{[(1-2\alpha) + \cos \theta_i]^2}{2(1+\cos^2 \theta_i)} \quad (5)$$

which has been obtained considering the crosstalk isolation and applying (15), with the polarization unit vector of the real antenna $\mathbf{p}_R' = (1/\sqrt{1+\cos^2 \theta}) \begin{pmatrix} \cos \theta \\ -1 \end{pmatrix}$ and $\mathbf{p}^w = (1/\sqrt{2}) \begin{pmatrix} 1 \\ -1 \end{pmatrix}$; the conjugate operator is required to transform the polarization unit vector of the transmitted field in the same reference system of the receiving antenna.

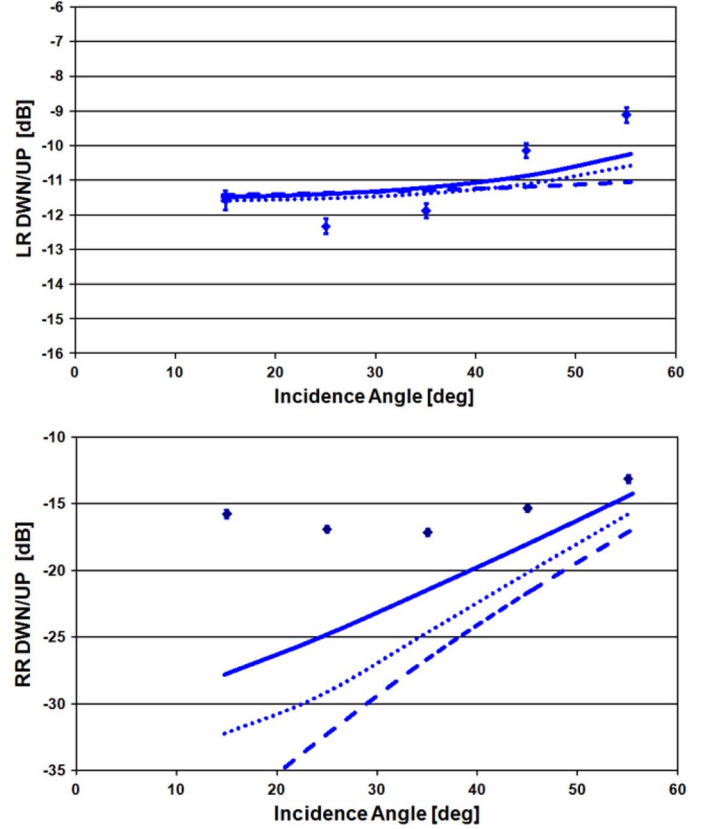


Fig. 6. SAVERS results obtained considering polarization mismatch with crosstalk effects of (dotted lines) -10 dB and (continuous lines) -20 dB and (dashed lines) without these effects compared to (circles with error bars) data measured during LEiMON over a bare soil field ($\sigma_z = 0.7$ cm, $\ell = 5$ cm, and $SMC = 10\%$). Top panel: LR signal. Bottom panel: RR signal.

The quantity measured, and simulated by SAVERS, is then the following ratio between the signals measured by the downward- and upward-looking antennas (DWN/UP):

$$\begin{aligned}(DWN/UP)_{rt} &= \frac{|Y_{rt}(\tau, f)|^2}{|Y_{RR}^{UP}|^2} \\ &= \frac{R_{TR}^2}{4\pi PLF^{UP} G_R(\theta_i)} \int_A \int \frac{G_R(\theta_s)}{R_R^2 R_T^2} \\ &\quad \times \sigma_{rt}^{0'}(\theta_i, \phi_i; \theta_s, \phi_s; \Theta) \Lambda^2(\delta\tau) S^2(\delta f) dA. \quad (6)\end{aligned}$$

The upward and downward antenna gains have been assumed to have the same cosinusoidal shape: $G_R(\theta) = G_0 \cos^n \theta$. In summary, when normalizing (1) by the quantity in (4), the common factor $\lambda^2 G_T(\theta_i) G_0 P_T T_i^2 / (4\pi)^2$ cancels out so that the DWN/UP normalization makes the LEiMON data and simulator output independent to variations of the power density at the Earth surface of the satellite signal, as well as to the maximum gain G_0 of the instrument antennas. Note also that the polarization mismatch and the crosstalk effects are included in (6) through the polarization loss factor (PLF^{UP}) for the upward signal and through the primed bistatic scattering coefficient $\sigma_{rt}^{0'}$ for the downward signal.

In Fig. 6, an example of SAVERS results concerning an ideal receiving antenna and results obtained including the

polarization mismatch and crosstalk are given. The simulations were performed considering a bare soil with roughness height standard deviation $\sigma_z = 0.7$ cm, correlation length $\ell = 5$ cm, and soil moisture content $\text{SMC} = 10\%$, corresponding to measurements acquired in late summer during the LEiMON experiment. It can be observed that the LR and RR normalized reflected signals have both an increasing trend versus the incidence angle, but the effects of crosstalk and polarization mismatch take place at different angles, depending on polarization. Indeed, it is well known that, given a right-polarized incident field, surface scattering gives rise mainly to a left-polarized wave, while right-polarized scattering becomes significant only when approaching the Brewster angle. The polarization mismatch combines the two components: the effect of polarization mismatch on LR signal is significant at large incidence angles, while on RR signal, it is significant at low incidence angles (compare continuous and dashed curves in Fig. 6). In both cases, polarization mismatch increases the normalized power represented in the plots in the considered angular range. We do not report the case corresponding to crosstalk absence since a crosstalk of -20 dB superimposes the case of $\alpha = 0$ (no crosstalk between receiver channels). The introduction of a crosstalk of -10 dB partially mitigates the effect of the mismatch in the considered angular range: with respect to the ideal case (no mismatch and no crosstalk), it produces a maximum increase of 1 dB at LR polarization and between 1 and 5 dB at RR, depending on the angle. Roughly speaking, the crosstalk redirects the right-polarized signal collected by the real left-polarized antenna toward the correct right channel.

During the LEiMON experiment, only reflected signals at incidence angles lower than 50° were acquired, in order to consider signals coming through the antenna main lobe and avoid multipath effects [10]. At these angles, polarization mismatch affects mostly the normalized RR signal. In Fig. 6, it is apparent that the consideration of the mismatch tends to improve the comparison between measurements and simulations at higher incidence angles. On the other hand, data reported in the bottom panel of Fig. 6 (as well as other LEiMON data published in [10]) show a large model underestimation at small angles. This can be due to an incorrect representation of the RR scattering by the AIEM, but as pointed out in [10], the limited sensitivity of the GNSS conventional receivers could introduce a saturation effect on reflected signals lower than a given threshold, corresponding to the noise floor. Also, the ellipticity of the emitted GPS signal, which was not taken into account in SAVERS, could contribute to enhance the right-polarized received signal (this effect will be investigated in the future). Indeed, the transmitted signal contains also a left-polarized component which could be depolarized by interaction with soil, thus leading to an enhanced right received signal. Due to the aforementioned reasons, only the LR signal will be taken into account in the following discussion.

In summary, the effects of polarization mismatch and crosstalk are not quantitatively important in the LEiMON experiment, where only the GPS satellites at high elevation were considered. They may become significant far from the antenna boresight at LR polarization and even at low incidence angles for receivers able to detect the weak RR signal.

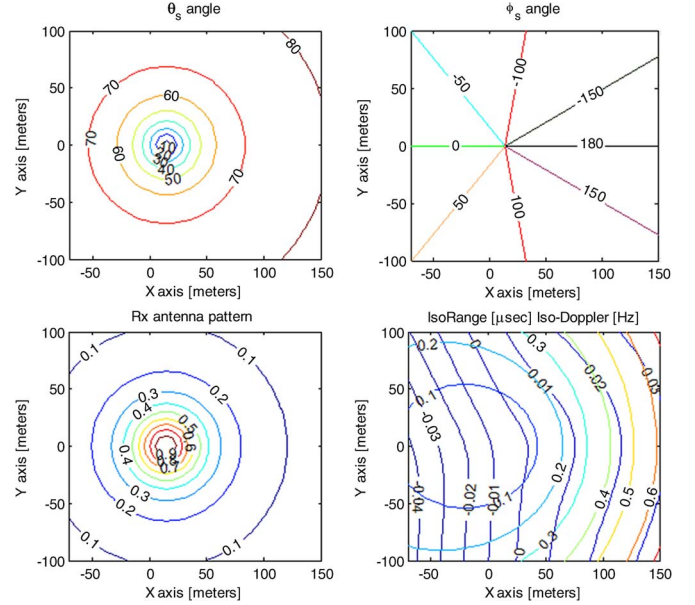


Fig. 7. Same as Fig. 7, but referring to the geometry of the LEiMON experiment. Receiver height = 25 m, receiver velocity = 0° m/s, antenna beamwidth = 100° , and incidence angle = 31.4° .

IV. COMPARISONS WITH LEiMON EXPERIMENTAL DATA

The configuration adopted in the LEiMON experimental setup was considered (a steady receiver at a 25-m height with an antenna beamwidth of 100°), in order to preliminarily compare the theoretical simulations provided by SAVERS with the data collected experimentally. An in-depth comparison of the whole LEiMON data set is beyond the scope of this paper, but this preliminary assessment provides significant indications on SAVERS performance and possible future developments.

First of all, we remark that the LEiMON measurements concern a beam-limited configuration since the antenna footprint covers an area of about 40-m diameter, smaller than the area resolved by the C/A code resolution (150–300-m diameter) and by the Doppler bandwidth Δf resulting from the cross-correlation processing (25 Hz, with $T_i = 20$ ms). This implies that the integral of (1) is performed over the whole antenna footprint and only one sample of the DDM is measured. This is displayed in Fig. 7 (bottom right plot) by the intermediate graphical output of SAVERS which plots the isodelay and iso-Doppler contour lines in the LEiMON configuration. It can be observed that the half-power antenna footprint (bottom left plot in Fig. 7) covers points with a delay smaller than $0.1 \mu\text{s}$ and Doppler shifts smaller than 0.02 Hz. This means that the chip and frequency modulation functions, i.e., Λ^2 and S^2 in (1) and (6), are equal to 1 within the integration domain and, as remarked previously, only the peak power is retained in this configuration.

As it is described in [10], the test site was divided into two parts along the North–South direction: the East and West sides, which were worked in two different ways during the campaign. In particular, the West side was seeded with sunflower plants growing from June to August. The surface roughness parameters were measured using the needle profilometer

TABLE I
DATES SELECTED FOR COMPARISON OF SAVERS RESULTS AND
EXPERIMENTAL DATA. SOIL MOISTURE AND SURFACE ROUGHNESS
CONDITIONS MEASURED ON GROUND ARE ALSO REPORTED

Dates	SMC [%]	σ_z [cm] EAST field	σ_z [cm] WEST field
April 8 th	30	3	2.
July 28 th	18	0.85	1.5
August 26 th	10	0.7	1.2

approximately every week and, in any case, each time the surface roughness changed due to works or heavy rainfalls. The measurements were carried out along parallel and perpendicular directions with respect to the rows. In order to compare the simulator outputs with the experimental measurements, three data sets were selected from the LEiMON campaign. They represent extreme situations: very rough and wet soil (April 8), very smooth and dry soil (August 26), and well-developed sunflower field with plant water content $PWC = 6.7 \text{ kg/m}^2$ (July 28). The selected dates and the corresponding ground-truth data, i.e., soil moisture content (SMC) and soil roughness height standard deviation (σ_z), are reported in Table I. The measured standard deviation of the heights has been used as input to SAVERS, whereas as far as the correlation length is concerned, its measurement is rather critical so that we decided to use the average measured value during the whole campaign $\ell = 5 \text{ cm}$. Although a limited number of examples is taken into account in this paper, they allowed us to verify the capability of SAVERS in reproducing the data and to address some critical aspects. In order to quantitatively evaluate the error of the model, it is necessary to carry out a statistically significant number of simulations, which is planned for the near future.

Fig. 8 reports the comparisons between experimental data (points represent mean values of all data acquired under the same incidence angle) and model simulations of DWN/UP values at LR polarization (continuous lines). The error bar reported in the figure is mainly a consequence of the signal fluctuations (speckle noise) affecting the individual measurements, which we have reduced by multilooking (incoherent averaging of the correlator outputs). Each data point refers to about $N = 100\text{--}200$ samples, processed with a coherent integration time of 20 ms. The error bars represent the standard deviation of the original samples divided by the square root of N .

Data concerning the West side of the Montespertoli field are represented by squares, while diamonds are used for the East side. In general, it is possible to observe that the model results reproduce the angular trend of the LEiMON data, even if there is an overestimation that increases with incidence angle. A crosstalk insulation of 20 dB (as indicated by the antenna manufacturer) was assumed in the simulations. It is noticeable that the relative difference between the experimental data of the East and West sides, which is related to the different conditions of the surface, is fairly well reproduced by the simulator. In April [see Fig. 8(a)], this difference is due to the different roughness of the two sides of the field: with the East one being rougher, it scatters lower power into the specular direction with respect to the West side. In July [see Fig. 8(b)], the West side is covered

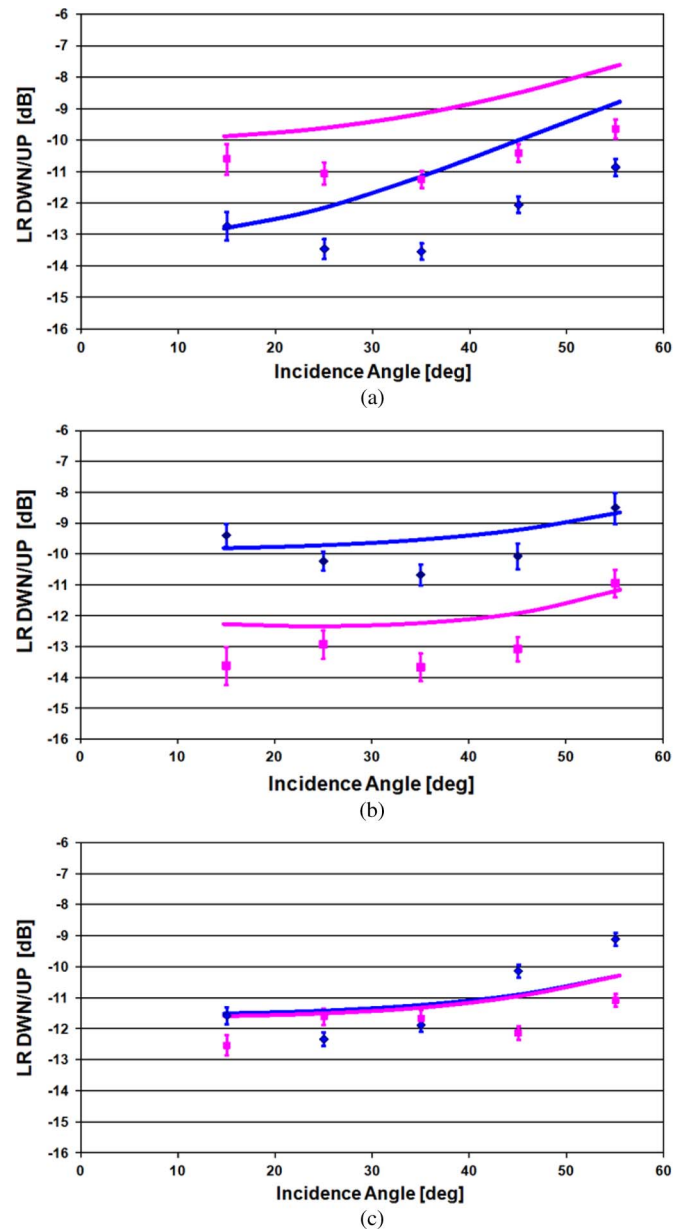


Fig. 8. Measured and simulated LR signal (normalized to the direct signal) as function of the incidence angle. (a) April 8, very rough and wet bare soil. (b) July 28, sunflower field on the West side and bare soil on the East side. (c) August 26, smooth and dry bare soil. Blue is assigned to East field, and magenta is assigned to West field. Continuous lines represent the theoretical results, and diamonds and squares represent the experimental data. Vertical bars represent the standard deviation of the individual multilook measurements.

by fully developed sunflower vegetation which attenuates soil scattering, while the East side is quite smooth, thus reflecting a stronger signal coherently. In August [see Fig. 8(c)], the two sides have very similar roughness, with the West one being slightly rougher. The East side is characterized by a similar roughness in July and August so that the difference between the two acquisitions must be related to the different SMC 's (see Table I), just as indicated by the simulator. We point out here that the increasing trend with incidence angle, observed in both experimental and theoretical data, although not perfectly matching, is attributed by the simulator to several causes, which contribute differently depending on the roughness

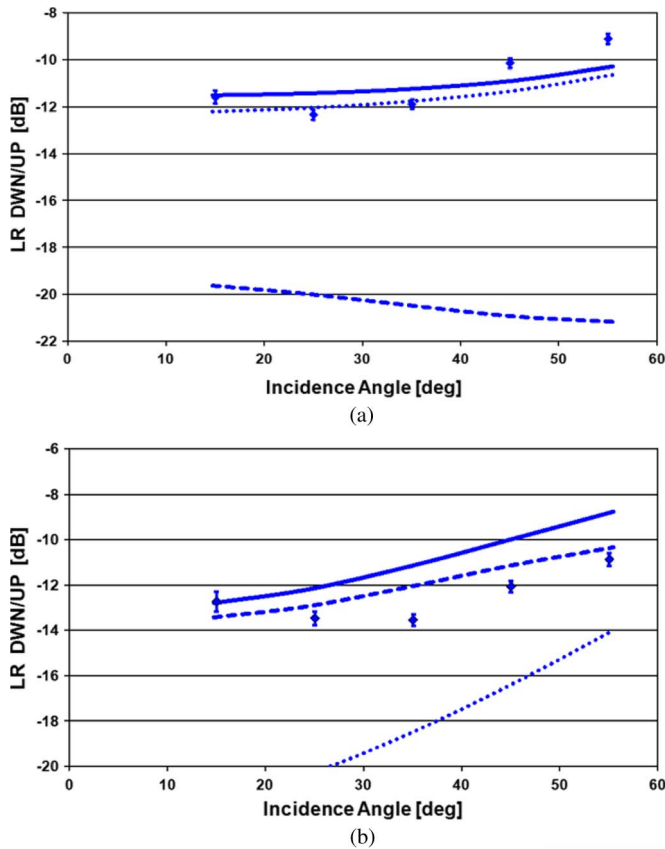


Fig. 9. (Dotted line) Coherent component and (dashed line) incoherent component of the (continuous line) total simulated LR signal normalized to the direct one. Diamonds are the measured normalized LR signal. (a) August 26, smooth field $\sigma_z = 0.7$ cm. (b) April 8, rough field $\sigma_z = 3$ cm.

of the surface, i.e., depending on the dominance of the coherent or incoherent component. It is worth to discuss this aspect, which may help in understanding the good matching of the angular trend of data and simulations in Fig. 8(b) and (c) with respect to Fig. 8(a).

The relative contribution of coherent and incoherent components of the signal detected by the instrument is singled out in Fig. 9, according to SAVERS results. If the surface is smooth, the signal is made up almost exclusively by the coherent component [see Fig. 9(a)], while the signal is almost completely incoherent if the surface is rough [see Fig. 9(b)]. Furthermore, according to model simulations, the angular trend of the coherent component is increasing, while the incoherent component shows different trends in the two cases. We remind that the reflected coherent component is concentrated around the specular direction (as it is well known and as it can be observed in the bottom plots of Figs. 3 and 4), i.e., the upward and downward signals impinge with the same angle on the two receiving antennas. It means that the normalization of (6) cancels out the antenna gain factors (the G_R 's) and highlights the increasing trend of the coherent reflected signal. The latter is proportional to the Fresnel reflectivity at LR polarization corrected by the roughness coefficient ($e^{-(2k\sigma_z \cos \theta)^2}$) and modified by the antenna polarization mismatch. Both effects give rise to the increasing trend with angle. In particular, the roughness coefficient increases faster when σ_z is large. When

the surface is smooth, also the incoherent component is peaked in the specular direction (see the upper plot of Fig. 3) so that, also in this case, $G_R(\theta_i) = G_R(\theta_s)$, and their effects cancel out in the normalized signal. As a consequence, the angular trend of the incoherent component in Fig. 9(a) reproduces mainly the one of the bistatic scattering coefficient $\sigma^0(\theta_i; \theta_s = \theta_i, \phi_s = \phi_i = 0)$ at LR polarization in the specular direction.

Conversely, incoherent scattering from the observed surface prevails when the surface is rough [see Fig. 9(b)]. Contrarily to the previous case, the downward-looking antenna collects power from all directions, i.e., coming from all scattering elements within the antenna footprint (see the upper right plot of Fig. 4), while the up-looking antenna receives power from one direction only (the one of the transmitting GPS). It follows that, although the two GNSS-R antenna gains are the same, their effects [i.e., the $G_R(\theta_i)$ and $G_R(\theta_s)$ terms in (6)] do not cancel out in the normalization procedure when incoherent scattering represents the dominant contribution. When the surface is rough, the incoherent scattering coefficient $\sigma^0(\theta_i, \phi_i; \theta_s, \phi_s)$ is substantially independent of the angle of incidence, and it remains high over the whole antenna footprint A . Aside from polarization mismatch, the increasing trend of the normalized signal versus incidence angle is significantly determined by the decreasing trend of the up-received signal $|Y_{RR}^{UP}|^2$. The latter diminishes with angle because of the decreasing antenna gain (we remind that the upward antenna is zenith pointing), letting the normalized DWN/UP signal increase. As a consequence, an incorrect representation of the up- and down-looking antenna gains, or even slight differences between the two, could cause the increasing discrepancy between experimental and simulated data versus incidence angle, which is, in fact, more apparent in the rough soil case of Fig. 9(b), when the two gains do not compensate in the normalization to the direct signal.

V. CONCLUSION

In this paper, a simulator (named SAVERS) capable of reproducing the GNSS signal reflected by the land surface and recorded through a cross-correlation processing has been presented. Its main features, the involved electromagnetic models, and the data which are outputted have been discussed. Then, the polarization synthesis technique, applied to take antenna polarization mismatch and cross-polarization isolation into account, has been presented. A subset of experimental data collected during the LEiMON project has been used to demonstrate the performance of the simulator to reproduce them in different scenarios, with different soil roughness and moisture content, as well as in the presence of vegetation cover. SAVERS has shown to be able to reproduce fairly well the different ground situations at LR polarization and low incidence angles. Less satisfactory results have been found in predicting the RR measured signal, which, however, could be due to the low sensitivity of the instrument which produces a saturation effect under a certain value. The polarization mismatch of real antennas has proved to be particularly important at RR polarization at low angles and at LR polarization at large angles ($> 40^\circ$). Finally, the simulations have shown that, in the

beam-limited configuration of the ground-based LEiMON campaign, both the coherent and the incoherent scattering contribute to the GNSS-R signal, but their relative weight depends on surface roughness. In particular, the simulations at large angles are sensitive to antenna gain when the signal is dominated by incoherent scattering.

For an ultimate validation of SAVERS and its theoretical assumptions, a more extensive data set is required. For this purpose, the exploitation of the whole LEiMON data set, and of data from an airborne campaign, is planned as a future work.

APPENDIX

A. Polarization Synthesis

We remind that the scattering matrix \mathbf{S} of the target relates the incident field \mathbf{E}^i to the scattered field \mathbf{E}^s by means of

$$\begin{aligned}\mathbf{E}^s &= \begin{pmatrix} E_p^s \\ E_q^s \end{pmatrix} = \frac{e^{-\iota k R}}{R} \begin{pmatrix} S_{pp} & S_{pq} \\ S_{qp} & S_{qq} \end{pmatrix} \begin{pmatrix} E_p^i \\ E_q^i \end{pmatrix} \\ &= \frac{e^{-\iota k R}}{R} \mathbf{S} \mathbf{E}^i\end{aligned}\quad (7)$$

where $k = 2\pi/\lambda$ is the wavenumber in free space and R is the distance between the scatterer and the receiving antenna. The scattering matrix elements depend on the incidence and scattering angles and on the target parameters, i.e., $S_{pq}(\theta_i, \phi_i; \theta_s, \phi_s; \Theta)$; however, here and in the following, this dependence has been understood. p and q represent two orthogonal components of the complex scattering field, generally corresponding to horizontal h or vertical v components (but potentially also right circular R or left circular L components, respectively). S_{pq} 's are complex quantities that describe the amplitude, phase, and polarization of the scattered wave.

In the BSA convention [29], computing the squared modulus and applying the ensemble average operator to derive the mean power density scattered from a random surface, the polarization synthesis allows defining the scattering coefficient as

$$\sigma_{rt}^0 = \frac{4\pi}{A} \langle |\mathbf{p}^r \cdot \mathbf{S} \mathbf{p}^t|^2 \rangle \quad (8)$$

where $\langle \dots \rangle$ indicates the ensemble average and parameter A is the surface scattering area already defined in (1). Finally, \mathbf{p}^r and \mathbf{p}^t are the polarization unit vectors of the receiving (r) antenna and transmitted (t) electromagnetic field. When the transmitting antenna radiates an ideal right circularly polarized wave and the receiving antenna is also ideal, either right ($\mathbf{p}_R^r = (1/\sqrt{2})(\begin{smallmatrix} 1 \\ -\iota \end{smallmatrix})$) or left ($\mathbf{p}_L^r = (1/\sqrt{2})(\begin{smallmatrix} 1 \\ \iota \end{smallmatrix})$) circularly polarized, it

is straightforward to derive the scattering coefficients since the polarization synthesis yields:

$$\begin{aligned}\sigma_{RR}^0 &= \frac{4\pi}{A} \left\langle \left| \frac{S_{vv} - S_{hh} - \iota(S_{vh} + S_{hv})}{2} \right|^2 \right\rangle = \frac{4\pi}{A} \langle |S_{RR}|^2 \rangle \\ \sigma_{LR}^0 &= \frac{4\pi}{A} \left\langle \left| \frac{S_{vv} + S_{hh} - \iota(S_{vh} - S_{hv})}{2} \right|^2 \right\rangle = \frac{4\pi}{A} \langle |S_{LR}|^2 \rangle.\end{aligned}\quad (9)$$

In (9), the harmonic time variability in the complex domain is assumed to be $e^{\iota\omega t}$. For a perfect electrical conductor $S_{hh} = S_{vv} = 1$, $S_{hv} = S_{vh} = 0$ so that the right-right (RR) scattering cross section is null and the left-right (LR) scattering cross section is equal to 4π , as expected.

Therefore, expliciting (9), we have to evaluate a set of terms of the type $\langle S_{pq} S_{mn}^* \rangle$. These terms form the so-called polarimetric Stokes (or Muller) matrix which is given by (10) shown at the bottom of the page, where \Re and \Im stand for the real part and imaginary part operators. It is apparent that the circularly polarized scattering coefficient can be derived from the fully polarimetric versions of the electromagnetic models mentioned in Section III, e.g., AIEM or Tor Vergata model. The latter, in particular, applies the vector radiative transfer theory to get the Stokes matrix of the whole soil-vegetation canopy [22].

B. Note on the Reference Frames

We remind that, to apply the polarization synthesis of (8) and (9), the scattering matrix must be defined in the BSA convention. As a consequence, when the scattering matrix is known in the *forward scattering alignment* (FSA) system (\mathbf{S}^{FSA}), the following transformation must be applied:

$$\mathbf{S} = \mathbf{S}^{BSA} = \begin{pmatrix} 1 & 0 \\ 0 & -1 \end{pmatrix} \mathbf{S}^{FSA}. \quad (11)$$

This is the case of the vegetation scattering matrix used in the Tor Vergata model. When considering the AIEM, to describe the scattering process, we remark that, in [23] and [30], the $\langle S_{pq}^{IEM} S_{mn}^{*IEM} \rangle$ elements of the Stokes matrix are derived neither in the FSA nor in the BSA convention, and the following transformation must be considered:

$$\begin{aligned}\mathbf{S} &= \mathbf{S}^{BSA} = \begin{pmatrix} 1 & 0 \\ 0 & -1 \end{pmatrix} \mathbf{S}^{IEM} \begin{pmatrix} 1 & 0 \\ 0 & -1 \end{pmatrix} \\ &= \begin{pmatrix} S_{vv}^{IEM} & -S_{vh}^{IEM} \\ -S_{hv}^{IEM} & S_{hh}^{IEM} \end{pmatrix}.\end{aligned}\quad (12)$$

$$\mathbf{M} = \begin{pmatrix} \langle |S_{vv}|^2 \rangle & \langle |S_{vh}|^2 \rangle & \Re \langle S_{vv} S_{vh}^* \rangle & -\Im \langle S_{vv} S_{vh}^* \rangle \\ \langle |S_{hv}|^2 \rangle & \langle |S_{hh}|^2 \rangle & \Re \langle S_{hv} S_{hh}^* \rangle & -\Im \langle S_{hv} S_{hh}^* \rangle \\ 2\Re \langle S_{vv} S_{hv}^* \rangle & 2\Re \langle S_{vh} S_{hh}^* \rangle & \Re \langle S_{vv} S_{hh}^* + S_{vh} S_{hv}^* \rangle & \Im \langle S_{vh} S_{hv}^* - S_{vv} S_{hh}^* \rangle \\ 2\Im \langle S_{vv} S_{hv}^* \rangle & 2\Im \langle S_{vh} S_{hh}^* \rangle & \Im \langle S_{vv} S_{hh}^* + S_{vh} S_{hv}^* \rangle & \Re \langle S_{vv} S_{hh}^* - S_{vh} S_{hv}^* \rangle \end{pmatrix} \quad (10)$$

C. Polarization Vectors of a Real Antenna

The scattering coefficients in (9) were obtained assuming that both the transmitter and receiver are ideal circularly polarized antennas. In order to account for a real device, it is necessary to find a reasonable expression for the polarization unit vector ($\mathbf{p}^{r'}$) (the primed apex stands for the “real” antenna polarization unit vector, to be distinguished from the “ideal” one), assuming that it is nominally either right or left polarized. To this aim, we need a model of the electromagnetic field radiated by the antenna in any direction. We have considered a simple circularly polarized antenna formed by two short (elementary) electric dipoles (which we may call a double-dipole antenna), orthogonal to each other and fed with a $\pm\pi/2$ phase shift. Depending on the sign of the phase shift, one can obtain a right or a left rotation of the electric field. Starting from the electromagnetic field of a short dipole, it is possible to find the field of a couple of dipoles lying in the xy plane, with maximum radiation along the z -axes. With respect to the xyz Cartesian coordinate frame, the unit vectors of the vertical \mathbf{v} and horizontal \mathbf{h} polarizations correspond to the unit vectors $\boldsymbol{\theta}$ and $\boldsymbol{\phi}$, associated to the zenith and azimuth angles in spherical coordinates, respectively.

After some algebraic manipulations, it is possible to get the polarization unit vectors of a real circularly polarized antenna formed by a couple of electrical dipoles as:

$$\begin{aligned}\mathbf{p}_L^{r'} &= \mathbf{p}_L^{rE} = \frac{1}{\sqrt{1 + \cos^2 \theta}} \begin{pmatrix} \cos \theta \\ \iota \\ 0 \end{pmatrix} \\ \mathbf{p}_R^{r'} &= \mathbf{p}_R^{rE} = \frac{1}{\sqrt{1 + \cos^2 \theta}} \begin{pmatrix} \cos \theta \\ -\iota \\ 0 \end{pmatrix}\end{aligned}\quad (13)$$

where superscript E stands for electric dipoles. We can see that the radiated field has a perfect left polarization (or right polarization) only along the boresight direction z , where zenith angle θ equals zero, and horizontal and vertical components of the field are identical and are shifted in phase of an angle equal to $\pi/2$ (or $-\pi/2$). Conversely, in any other direction, the polarization is elliptical, departing from the circular one for increasing zenith angle (far from the boresight direction). The polarization unit vectors of a pair of magnetic dipoles have been also derived in the same way, obtaining $\mathbf{p}_L^{rM} = (1/\sqrt{1 + \cos^2 \theta}) \begin{pmatrix} 1 \\ \iota \cos \theta \\ 0 \end{pmatrix}$ and $\mathbf{p}_R^{rM} = (1/\sqrt{1 + \cos^2 \theta}) \begin{pmatrix} 1 \\ -\iota \cos \theta \\ 0 \end{pmatrix}$. For the sake of conciseness, only the electric double dipole is considered here since the final results of this paper are not significantly different even assuming a pair of magnetic dipoles.

D. Polarization Mismatch

The same “real” scattering coefficients can be found if they are calculated through

$$\sigma_{rt}^{0r} = \frac{4\pi R^2}{A} \frac{P^r}{P^i} \quad (14)$$

where $P^i = |\mathbf{E}^i|^2/2\eta$ is the power density incident on area A (η is the intrinsic impedance of the medium where the wave propagates) and P^r is the power density received by the antenna. The latter is related to the power density $P^s = |\mathbf{E}^s|^2/2\eta$

scattered toward the antenna itself by the target, through the polarization loss factor of the down-looking antenna PLF^{DN} [30]

$$P^r = PLF^{DN} \cdot P^s \text{ with } PLF^{DN} = \left| \mathbf{p}^{r'} \cdot \mathbf{p}^w \right|^2 \quad (15)$$

where $\mathbf{p}^{r'}$ is the polarization unit vector of the real receiving antenna, defined in (13), and \mathbf{p}^w is the polarization unit vector of the field impinging on the antenna. In the case of the down-looking antenna, $\mathbf{p}^w = \mathbf{E}^s/|\mathbf{E}^s|$ (note that both $\mathbf{p}^{r'}$ and \mathbf{p}^w are defined in the BSA system).

E. Polarization Crosstalk

Assuming that a fraction α (less than one and possibly small) of the right-polarized signal goes into the left-polarized receiving chain and vice versa, we can model the measured scattering coefficient, including polarization mismatch and antenna polarization crosstalk, again by the polarization synthesis expressed as in the following:

$$\begin{aligned}\sigma_{LR}^{0r} &= \frac{4\pi}{A} \left\langle \left| \left(\alpha \mathbf{p}_R^{r'} + (1 - \alpha) \mathbf{p}_L^{r'} \right) \cdot \mathbf{S} \mathbf{p}_R^t \right|^2 \right\rangle \\ \sigma_{RR}^{0r} &= \frac{4\pi}{A} \left\langle \left| \left(\alpha \mathbf{p}_L^{r'} + (1 - \alpha) \mathbf{p}_R^{r'} \right) \cdot \mathbf{S} \mathbf{p}_R^t \right|^2 \right\rangle\end{aligned}\quad (16)$$

where $(1 - \alpha)$ is the fraction of the signal which goes in the right channel, and the incident field is assumed again as a pure right-polarized one.

REFERENCES

- [1] N. Pierdicca, L. Pulvirenti, F. Ticconi, and M. Brogioni, “Radar bistatic configurations for soil moisture retrieval: A simulation study,” *IEEE Trans. Geosci. Remote Sens.*, vol. 46, no. 10, pp. 3252–3264, Oct. 2008.
- [2] L. Guerriero, N. Pierdicca, L. Pulvirenti, and P. Ferrazzoli, “Use of satellite radar bistatic measurements for crop monitoring: A simulation study,” *Remote Sens.*, vol. 5, no. 2, pp. 864–890, Feb. 2013.
- [3] N. J. Willis, *Bistatic Radar*. Boston, MA, USA: Artech House, 1991.
- [4] N. Pierdicca, L. De Titta, L. Pulvirenti, and G. della Pietra, “Bistatic radar configuration for soil moisture retrieval: Analysis of the spatial coverage,” *Sensors*, vol. 9, no. 9, pp. 7250–7265, Sep. 2009.
- [5] V. U. Zavorotny, D. Masters, A. Gasiewski, B. Bartram, S. Katzberg, P. Axelrad, and R. Zamora, “Seasonal polarimetric measurements of soil moisture using tower-based GPS bistatic radar,” in *Proc. IEEE Int. Geosci. Remote Sens. Symp.*, 2003, vol. 2, pp. 781–783.
- [6] D. Masters, P. Axelrad, and S. Katzberg, “Initial results of land-reflected GPS bistatic radar measurements in SMEX02,” *Remote Sens. Environ.*, vol. 92, no. 4, pp. 507–520, Sep. 2004.
- [7] S. J. Katzberg, O. Torres, M. S. Grant, and D. Masters, “Utilizing calibrated GPS reflected signals to estimate soil reflectivity and dielectric constant: Results from SMEX02,” *Remote Sens. Environ.*, vol. 100, no. 1, pp. 17–28, Jan. 2006.
- [8] A. Egido, G. Ruffini, M. Caparrini, C. Martin, E. Farres, and X. Banque, “Soil moisture monitoring using GNSS reflected signals,” *IST Colloquium Scientific and Fundamental Aspects of the Galileo Programme*, 7 pp., May 2008.
- [9] N. Rodríguez-Álvarez, A. Camps, M. Vall-llossera, X. Bosch-Lluis, A. Monerris, I. Ramos-Pérez, E. Valencia, J. F. Marchán-Hernandez, J. Martínez-Fernandez, G. Baroncini-Turicchia, C. Pérez-Gutiérrez, and N. Sanchez, “Land geophysical parameters retrieval using interference pattern GNSS-R technique,” *IEEE Trans. Geosci. Remote Sens.*, vol. 49, no. 1, pp. 71–84, Jan. 2011.
- [10] A. Egido, M. Caparrini, G. Ruffini, S. Paloscia, E. Santi, L. Guerriero, N. Pierdicca, and N. Floury, “GNSS-R for land bio-geophysical parameters monitoring: The LEIMON project,” in *Proc. Workshop GNSS Reflectometry*, 2010, pp. 1–33.
- [11] V. U. Zavorotny and A. G. Voronovich, “Scattering of GPS signals from the ocean with wind remote sensing application,” *IEEE Trans. Geosci. Remote Sens.*, vol. 38, no. 2, pp. 951–964, Mar. 2000.

- [12] V. U. Zavorotny and A. G. Voronovich, "Bistatic GPS signal reflections at various polarizations from rough land surface with moisture content," in *Proc. IEEE Int. Geosci. Remote Sens. Symp.*, 2000, vol. 7, pp. 2852–2854.
- [13] P. Beckman and A. Spizzichino, *The Scattering of Electromagnetic Waves from Rough Surfaces*. Norwood, MA, USA: Artech House, 1963.
- [14] F. T. Ulaby, R. K. Moore, and A. K. Fung, *Microwave Remote Sensing: Active and Passive*, vol. II. Dedham, MA, USA: Artech House, 1982.
- [15] L. Tsang, J. A. Kong, and R. T. Shin, *Theory of Microwave Remote Sensing*. Hoboken, NJ, USA: Wiley, 1985.
- [16] P. Ferrazzoli, L. Guerriero, N. Pierdicca, and R. Rahmoune, "Forest biomass monitoring with GNSS-R: Theoretical simulations," *Adv. Space Res.*, vol. 47, no. 10, pp. 1823–1832, May 2011.
- [17] A. Egido, M. Caparrini, L. Guerriero, N. Pierdicca, S. Paloscia, E. Santi, and M. Brogioni, "LEIMON Land Monitoring With Navigation Signals," ESA/ESTEC, Noordwijk, Netherlands, Final Rep. ESA Contract 22117/08/NL/AF, 2011.
- [18] S. Gleason, S. Hodgart, Y. Sun, C. Gommenginger, S. Mackin, M. Adjrad, and M. Unwin, "Detection and processing of bistatically reflected GPS signals from low earth orbit for the purpose of ocean remote sensing," *IEEE Trans. Geosci. Remote Sens.*, vol. 38, no. 6, pp. 1229–1241, Jun. 2005.
- [19] M. Caparrini, "Using reflected GNSS signals to estimate surface features over wide ocean areas," ESTEC, Noordwijk, Netherlands, ESTEC Rep. 2003, 1998.
- [20] G. A. Hajj and C. Zuffada, "Theoretical description of a bistatic system for ocean altimetry using the GPS signal," *Radio Sci.*, vol. 38, no. 5, pp. 10.1–10.19, Oct. 2003.
- [21] M. Brogioni, S. Pettinato, G. Macelloni, S. Paloscia, P. Pampaloni, N. Pierdicca, and F. Ticconi, "Sensitivity of bistatic scattering to soil moisture and surface roughness of bare soils," *Int. J. Remote Sens.*, vol. 31, no. 15, pp. 4227–4255, May 2010.
- [22] M. Bracaglia, P. Ferrazzoli, and L. Guerriero, "A fully polarimetric multiple scattering model for crops," *Remote Sens. Environ.*, vol. 54, no. 3, pp. 170–179, Dec. 1995.
- [23] T.-D. Wu and K.-S. Chen, "A reappraisal of the validity of the IEM model for backscattering from rough surfaces," *IEEE Trans. Geosci. Remote Sens.*, vol. 42, no. 4, pp. 743–753, Apr. 2004.
- [24] A. K. Fung and H. J. Eom, "Coherent scattering of a spherical wave from an irregular surface," *IEEE Trans. Antennas Propag.*, vol. AP-31, no. 1, pp. 68–72, Jan. 1983.
- [25] H. J. Eom and A. K. Fung, "A scatter model for vegetation up to K_u -band," *Remote Sens. Environ.*, vol. 15, no. 3, pp. 185–200, Jun. 1984.
- [26] M. A. Karam and A. K. Fung, "Electromagnetic scattering from a layer of finite length, randomly oriented, dielectric, circular cylinders over a rough interface with application to vegetation," *Int. J. Remote Sens.*, vol. 9, no. 6, pp. 1109–1134, Jun. 1988.
- [27] M. C. Dobson, F. T. Ulaby, M. T. Hallikainen, and M. A. El-Rayes, "Microwave dielectric behavior of wet soil—Part II: Dielectric mixing models," *IEEE Trans. Geosci. Remote Sens.*, vol. GRS-23, no. 1, pp. 35–45, Jan. 1985.
- [28] F. T. Ulaby and M. A. El-Rayes, "Microwave dielectric spectrum of vegetation—Part II: Dual dispersion model," *IEEE Trans. Geosci. Remote Sens.*, vol. 25, no. 5, pp. 550–556, Sep. 1987.
- [29] F. T. Ulaby and C. Elachi, *Radar Polarimetry for Geoscience Applications*. Boston, MA, USA: Artech House, 1990.
- [30] A. K. Fung, *Microwave Scattering and Emission Models and Their Applications*. Boston, MA, USA: Artech House, 1994.
- [31] C. A. Balanis, *Antenna Theory: Analysis and Design*. Hoboken, NJ, USA: Wiley, 1982.

Nazzareno Pierdicca (M'04–SM'13) received the Laurea (Doctor's) degree (*cum laude*) in electronic engineering from the Sapienza University of Rome, Rome, Italy, in 1981.

In 1978–1982, he worked for the Italian Agency for Alternative Energy (ENEA). From 1982 to 1990, he has been working in the Remote Sensing Division of Telespazio, Rome, Italy. In November 1990, he joined the Department of Information, Electronic and Telecommunication Engineering, Sapienza University of Rome. He is currently a Full Professor and teaches remote sensing and electromagnetic fields at the Faculty of Engineering, Sapienza University of Rome. His research activity mainly concerns electromagnetic scattering and emission models for sea and bare soil surfaces and their inversion, microwave radiometry of the atmosphere, and radar land applications.

Prof. Pierdicca is a member of the IEEE Geoscience and Remote Sensing Society (GRSS) and a past Chairman of the GRSS Central Italy Chapter.

Leila Guerriero (M'11) received the Laurea degree in physics from the Sapienza University of Rome, Rome, Italy, in 1986 and the Ph.D. degree in electromagnetism from the University of Rome Tor Vergata, Rome, Italy, in 1991.

Since 1994, she has been a Permanent Researcher at the University of Rome Tor Vergata, where she is currently an Associate Professor holding a course on Earth Satellite Monitoring. Her activities are mainly concerned on modeling microwave scattering and emissivity from agricultural and forested areas. She participated in several international projects, among them are the following: In 1988, she was involved in a cooperation between the Jet Propulsion Laboratory, Pasadena, CA, USA, and the Italian National Research Council for investigations on geophysical applications of Imaging Spectrometry in InfraRed and Visible Remote Sensing. In 1995, she participated in the ESA project on Radiometric Polarimetry of ocean surfaces. In 1999–2001, she participated in the European Community concerted action ERA-ORA whose objective was to improve radar data analysis and utilization. More recently, she has been part of the teams of the ESA projects "Soil Moisture and Ocean Salinity Satellite," "Development of SAR inversion algorithms for land applications," "Use of Bistatic Microwave Measurements for Earth Observation," "LEIMON: Land monitoring with navigation signals," and "GRASS: GNSS-Reflectometry Analysis for Biomass Monitoring."

Prof. Guerriero is a member of the Scientific Committee of MicroRad.

Roberto Giusto received the degree in electronic engineering with full marks and honors and the Research Doctorat (Ph.D.) degree in electronic engineering from the Sapienza University of Rome, Rome, Italy, in 1979 and 1991, respectively.

He has been a Radar Systems Analyst with Selenia S.p.A. and an Antenna System Engineer with Selenia Spazio S.p.A. He has been with URMET Telecommunications S.p.A. as a Research Director (1998–2004), and presently, he is running a small consultancy business as Project Manager and System Engineer in the fields of ICT and Remote Sensing, Wireless Communications, and Greenpower engineering.

Marco Brogioni (S'05–M'09) was born in Siena, Italy, in 1976. He received the degree in engineering from the University of Siena, Siena, Italy, in 2003 and the Ph.D. degree in remote sensing from the University of Pisa, Pisa, Italy, in 2008.

Since 2004, he has been with the Istituto di Fisica Applicata, Consiglio Nazionale delle Ricerche (CNR-IFAC), Sesto Fiorentino, Italy, working in the Microwave Remote Sensing Group. In 2006 and 2007, he has been a visitor student at the University of California, Santa Barbara, CA, USA. In 2008, he was selected by the AXA Research Fund for a postdoctoral grant about the study of the snow temperature evolution in Antarctica. In 2009, he obtained the renewal of the AXA fellowship for a second year. His research deals with passive and active microwave remote sensing applied to snow by using satellite (AMSR-E, Special Sensor Microwave/Imager, ASAR, Quikscat, and Soil Moisture and Ocean Salinity) and ground-based data. Moreover, his studies concern the development of electromagnetic models for passive and active microwave remote sensing of snow, soil, and vegetation.

Alejandro Egido received the five-year B.Sc. degree academic program in electrical engineering from the University of Zaragoza, Zaragoza, Spain. He developed his final research project in the Technical University of Dresden, Dresden, Germany, on the topic of leaky wave antennas over microstrip line. He received the Ph.D. degree from the Polytechnic University of Catalonia, Barcelona, Spain.

He has been stagier at the European Space Agency, where he worked in the Sentinel-1 ERS project, performing the interference analysis of the synthetic aperture radar instrument. Currently, he is working as a Scientific Researcher at Starlab, Barcelona. His main research field is the use of Global Navigation Satellite System signals as a source of opportunity for remote sensing applications and the development of the PARIS concept.